

Article

Performance Assessment of an Ice-Production Hybrid Solar CPV/T System Combining Both Adsorption and Vapor-Compression Refrigeration Systems

Mahmoud Badawy Elsheniti ^{1,2,*}, Abdulrahman AlRabiah ¹, Hany Al-Ansary ^{1,3}, Zeyad Almutairi ^{1,3,4}, Jamel Orfi ^{1,3} and Abdelrahman El-Leathy ^{1,5}

- ¹ Mechanical Engineering Department, College of Engineering, King Saud University, Riyadh 11451, Saudi Arabia
² Mechanical Engineering Department, Faculty of Engineering, Alexandria University, Alexandria 21544, Egypt
³ K.A.CARE Energy Research and Innovation Center at Riyadh, King Saud University, Riyadh 11451, Saudi Arabia
⁴ Sustainable Energy Technologies Center, College of Engineering, King Saud University, Riyadh 11451, Saudi Arabia
⁵ Mechanical Power Engineering Department, Faculty of Engineering, El-Mataria, Helwan University, Cairo 11718, Egypt
* Correspondence: mbadawy.c@ksu.edu.sa

Abstract: The technology of a hybrid solar concentration photovoltaic/thermal (CPV/T) system is an efficient way of converting solar energy to heat and electrical power, in which overall energy-extraction efficiency is at its highest. In this study, numerical dynamic simulation models were developed for a hybrid solar CPV/T system and an adsorption refrigeration system (ARS). Under the climatic conditions of Riyadh all year round, the electrical and thermal powers generated by the CPV/T system were used to estimate the ice production of both the vapor compression refrigeration system (VCS) and the ARS. The CPV/T system can provide a thermal energy of 37.6 kWh and electrical energy of 24.7 kWh a day on average over the year using a 12.5 m² facing area of Fresnel lenses. The ARS employed an advanced approach which used Maxsorb III adsorbent packed in two aluminum foam beds. An optimum cycle time of the ARS was adapted for each month to match the variation in the thermal energy, while a variable-speed compressor was chosen for the VCS. Due to its higher coefficient of performance (COP), the proposed solar hybrid system can produce 494.4 kg of ice per day while sharing 84.5% of the VCS. The average solar COP over the year of the hybrid system can attain 0.875, which represents a promising value for a solar ice-production system.

Keywords: solar concentration; photovoltaic thermal; adsorption ice production; solar COP; metal foam



Citation: Elsheniti, M.B.; AlRabiah, A.; Al-Ansary, H.; Almutairi, Z.; Orfi, J.; El-Leathy, A. Performance Assessment of an Ice-Production Hybrid Solar CPV/T System Combining Both Adsorption and Vapor-Compression Refrigeration Systems. *Sustainability* **2023**, *15*, 3711. <https://doi.org/10.3390/su15043711>

Academic Editors: Hassan M. Hussein Farh, Saad Mekhilef, Ahmed Fathy and Abdullrahman Abdullah Al-Shamma'a

Received: 10 January 2023
Revised: 10 February 2023
Accepted: 15 February 2023
Published: 17 February 2023



Copyright: © 2023 by the authors. Licensee MDPI, Basel, Switzerland. This article is an open access article distributed under the terms and conditions of the Creative Commons Attribution (CC BY) license (<https://creativecommons.org/licenses/by/4.0/>).

1. Introduction

Renewable energy is becoming a favorable source of energy around the world and in Saudi Arabia in particular, as it is considered environmentally friendly with no pollution to the atmosphere. The utilization of such an energy source aims to reduce fossil-fuel consumption and reduce CO₂ emissions. Solar radiation is considered one of the world's largest energy sources and utilizing that radiation to produce energy will reduce reliance on fossil fuels. Saudi Arabia's geographical location is strategic, as it sits in the center of the so-called "Sun Belt" and has a clear sky year round, which has made it a perfect site for utilizing solar energy [1]. The country is blessed with a huge amount of sunlight, receiving an average thermal energy of 2200 kWh/m² per year [2]. About 52 percent of the electricity produced in Saudi Arabia is used by the residential sector [3]; about 70 percent of this consumption is ascribed to refrigeration systems [4]; the bulk of these systems are run using a vapor-compression technique. The adsorption refrigeration system (ARS) presents a chance to use solar energy using the heat produced by solar radiation or

waste heat to produce the needed cooling. The concentrated photovoltaic (CPV) method is an example of harnessing solar energy and is an appropriate application where solar energy may be utilized to run an ARS. Several researchers have studied solar-operated ARSs and have identified several gaps and opportunities to be explored further to achieve practical applications of ARSs [5]. Some of these challenges include the system's poor coefficient of performance (COP) [6], the fact that it can only be used during the day, the low refrigeration capacity per mass of adsorbent, and the size of the system in comparison to a vapor-compression refrigeration system (VCS) with an equivalent capacity. On the other hand, VCS, which is typically powered by electricity generated by the combustion of fossil fuels, has a high COP, allowing it to dominate global markets. Due to the disparity between ARS and VCS, many studies have been conducted to combine both refrigeration systems in various configurations in order to maximize their benefits while minimizing their drawbacks [7].

An experimental analysis of a solar adsorption ice-maker system using a working pair of activated carbon and methanol with a 1000 mm × 800 mm solar collector was reported by Attalla et al. in [8]. According to the study, the system COP was approximately 0.146. In Kunming, China, Luo et al. [9] conducted year-round experimental evaluations of a solar adsorption ice maker using activated-carbon-methanol as the adsorption pair. The experiment revealed that the system's COP ranged from 0.08 to 0.127, and it produced 3.2 to 6.5 kg/m² of ice. According to Wang et al. [10], the COP and cooling capacity of the ARS can be improved by enhancing the mass transfer during the desorption process using a micro vacuum pump positioned between the adsorbent bed and the condenser. The pump was employed to reduce the condenser pressure during the desorption stage by exhausting the vapor desorbed. The study revealed that the maximum COP was 0.142 and the average COP of the improved model increased by 35.9% in comparison to the ARS with a natural mass circulation. Ambarita and Kawai [11] evaluated a solar-powered ARS with a bed filled with various adsorbents. According to the experimental study, the system with a pure activated carbon and methanol pair produced a higher COP than the system with a mixed activated alumina and activated carbon adsorbent at different ratios. The significant heat losses from the solar collector and the low heat transfer coefficient from the adsorber plate to the generator were the main causes of the overall low COP for all trials (the maximum average COP was 0.074). Elsheniti et al. [12] quantitatively analyzed the use of an aluminum fumarate and silica gel as adsorbents in a solar adsorption cooling and desalination system. The results showed that for normal cooling with inlet chilled water of 15 °C, the COP and gross COP_{solar} for the SG-based system reached 0.6 and 0.4, respectively; they were greater than those for the AF-based system due to the MOF aluminum fumarate's poor heat conductivity. As a result, improving heat and mass transmission in the adsorbent beds is crucial to enhancing the ARS's overall performance. One of the recently suggested methods in the literature that has to be investigated at the solar-driven ARS level is the use of superior adsorbent materials such as Maxsorb III combined with advanced foamed beds [13].

To collect both electrical and thermal energy from PV cells without focusing solar irradiation, the flat-plate PV/T hybrid system was introduced. Based on weather data from Alexandria, Egypt, Gado et al. [14] evaluated a PV/T hybrid adsorption-vapor compression refrigeration system for cooling applications and found that it can save about 30.7 percent of electrical energy. Using the combined air-water cooling technique suggested by Aghakhani and Afrand [15], a maximum total efficiency of 81.61 percent was achieved in a PV/T system. The concentrated photovoltaic/thermal (CPV/T) combination system has been developed to further enhance the flat-plate PV/T approach through an optical concentrator. In contrast to conventional PV/T, the CPV/T technology uses an imaging or non-imaging optical concentrator as the reflector to obtain high-intensity irradiation in a considerably smaller solar-cell receiver [16]. The development of an effective solar (CPV/T) system with appropriate use of the generated power by merging several technologies has also been the subject of numerous studies [17]. The cells' maximum temperature of 110 °C, depending

on the available varieties in the global market, controls the temperature level of the thermal power produced by the CPV/T system. As a result, the system's exit fluid temperature is often below 100 °C, producing low-grade thermal energy that some technologies can use. Different solar cogeneration systems, including the organic Rankine cycle [18], absorption and adsorption systems [19,20], solar desiccant cooling, and combined heat and power systems [21], have been the focus of many studies.

A 2-D computational model for the fluid cooling passage combined with a thermal resistance model for the remaining parts of a CPV/T module was built by Xu and Kleinstreuer [22]. When using nanofluids and aiming for thermal energy at a temperature of about 62 °C, the overall efficiency of 70% includes contributions from electrical and thermal systems of 11% and 59%, respectively. A CPV/T system combined with an integrated adsorption-organic cycle for normal cooling, desalination, and power generation was examined numerically under three different scenarios in the work carried out by Albaik et al. [19]. The CPV/T used a multijunction solar-cell assembly on top of a cooling channel and a Fresnel-lens concentrator. The studies were carried out at 1000 W/m² of solar irradiation. Maximum energy conversion efficiency for the entire system was 68.47 percent. A CPV/T system with an integrated small-scale ORC was examined by Alamri et al. [23], utilizing various working fluids. According to their findings, the system converted solar energy into electricity with a total efficiency of 46.57 percent when R245fa was used as the working fluid. Buonomano et al. [24] explored the combination of adsorption and absorption chillers with CPV/T systems and flat PV/T collectors. A thermodynamic-based model was developed for the dynamic simulation of several locations in Europe. They concluded that the adsorption chiller should be used if the thermal performance of the solar collectors is subpar. In addition, the usage of an electric VCS as a backup device yields the highest simultaneous energy and cost-effective performance in all the analyzed weather zones and for all the simulated system designs.

The current paper presents a novel simulated case study on the production of ice using an integrated solar refrigeration system composed of a CPV/T system that drives both ARS and VCS to operate simultaneously throughout the year using Riyadh climate data. By delivering cooling during the day and night, the solar ice maker proposed in this study can serve as an alternative to solar cooling systems that are intermittent. For the CPV/T system, a transient three-dimensional CFD model is created to mimic its performance over the course of a year. A lumped parameter model for the ARS is developed to simulate the newly emerging aluminum-foam beds packed with the advanced Maxsorb III adsorbent and coupled with the condenser and evaporator submodels [25]. The ARS model is used to determine the design parameters to match the available thermal power produced by the CPV/T system and optimize ARS's cycle time. In addition, a commercially available variable-speed VCS is chosen to utilize the electricity generated by the CPV/T system. A monthly-based simulation is introduced in this study to predict the ice production from both refrigeration subsystems and show the overall performance of the integrated system. To obtain more pertinent results, the study considers the different types of losses to evaluate the proposed hybrid system and report the energy balance sheet.

2. Methodology

The schematic diagram of the proposed hybrid solar CPV/T system, which drives both the adsorption refrigeration system (ARS) and the vapor compression refrigeration system (VCS) is shown in Figure 1. The electrical power drives the motor-operated compressor in the VCS, and the extracted thermal power heats up the adsorbent bed in the ARS to desorb the refrigerant from the adsorbent. Both the ARS and VCS systems are simultaneously used to produce ice. The method used in the study entails creating a 3-D CFD model for the CPV/T system first, then using the results to develop and choose the parameters required for the integrated system for each component under the real weather conditions in Riyadh.

The refractive prisms, which shape the Fresnel lens, focus the incident rays on the receiver based on the focal length of the lens. The prisms' geometry can be described mathematically using the following equations [27,28]:

$$n \sin(\alpha) = \sin(\theta) \quad (1)$$

$$\tan(\theta - \alpha) = \frac{R}{f} \quad (2)$$

$$\tan(\alpha) = \frac{R}{n\sqrt{R^2 - f^2} - f} \quad (3)$$

where R is the distance between incident light and the optical axis, f is the focal length of a Fresnel lens, α is the prism angle, θ is an angle between the refractive ray and the perpendicular direction to the prism surface, and n is the refractive index. The Fresnel-lens parameters are listed in Table 1.

Table 1. Fresnel-lens parameters [29].

Parameter	Value
Fresnel-lens area (mm ²)	230 mm × 230 mm
Focal length	220 mm
Thickness	5 mm
Groove pitch	0.5 mm
Transmissivity (%)	92%

The active area of the Fresnel-lens aperture is 230 mm × 230 mm (0.0529 m²). Hence, the resulting geometrical concentration ratio (GCR) is 529X, which is the maximum concentration ratio (CR) that can be achieved if no optical losses occurred. However, this GCR can be controlled by adjusting the aperture area of the Fresnel lens [30].

$$GCR = \frac{A_{Lens}}{A_{Cell}} \quad (4)$$

$$CR = \frac{A_{Lens}}{A_{Cell}} \eta_{Opt} \quad (5)$$

where GCR is the geometrical concentration ratio, A_{Lens} is the aperture area of the Fresnel lens, A_{Cell} is the CPV cell area (receiver area), and η_{Opt} is the optical efficiency of the Fresnel lens.

Numerical Simulation of the CPV/T Assembly

Using COMSOL Multiphysics, the CPV/T assembly was mathematically investigated and simulated. Three physics were employed in COMSOL Multiphysics to carry out the simulation. The first is the geometrical optics physics, which is needed to carry out the ray-tracing simulation. The second one involves studying the heat transmission of the CPV/T system using solids and fluids physics. The cooling fluid used in the heat sink beneath the CPV cell is simulated using turbulent flow physics.

Two coupling multiphysics are also utilized to connect the chosen physics. The link between geometrical optics, heat-transfer interfaces, and non-isothermal flow is made using the ray heating physics. The flow is not isothermal. The interfaces between the physics of heat transport and turbulent flow are coupled via non-isothermal multiphysics. Fresnel equations and Snell's laws were utilized in geometrical optics physics to model and simulate ray tracing for the CPV/T as follows [31]:

$$\frac{d\mathbf{k}}{dt} = -\frac{\partial\omega}{\partial q_{solar}} \mathbf{k} = x, y, z \quad (6)$$

$$\frac{dq_{solar}}{dt} = -\frac{\partial\omega}{\partial k} \mathbf{k} = x, y, z \quad (7)$$

where \mathbf{k} is the 3D ray vector, t is the time, ω is the angular frequency, and q_{solar} is the position vector.

Due to their efficiencies, the solar radiation energy received by the CPV cells is not fully converted to electrical power. To calculate the amount of energy that is converted to heat by the cells, Equation (8) can be used [32].

$$q_{heat} = q_{rad} (1 - \eta_{CPV}) CR \quad (8)$$

where CR is the concentration ratio, q_{rad} is the direct solar-radiation incident on each CPV cell, and η_{CPV} is the CPV cell electrical efficiency, which is a function of the cell operating temperature and can be calculated using Equation (9) [33].

$$\eta_{CPV} = \eta_{ref} (1 - \beta_{thermal} (T_{CPV} - T_{ref})) \quad (9)$$

where η_{ref} is the reference cell efficiency and $\beta_{thermal}$ is cell-efficiency coefficient. The heat generated from the solar radiation and dissipated into the CPV cell is conducted from the top solid layers of the cell to the heat sink by a conduction heat-transfer mechanism that can be expressed by Fourier's law.

$$q_{cond} = -k_{cond} \nabla T \quad (10)$$

where k_{cond} is the thermal conductivity of the material and q_{cond} is the conduction heat transfer. To consider the heat loss from the assembly to the ambient air by convection, Equation (11) is used.

$$Q_{conv} = h A (T_{surf} - T_{amp}) \quad (11)$$

where Q_{conv} is the convective heat-transfer rate, A is the surface area exposed to the ambient, and h the heat-transfer coefficient by convection, which was fixed to $10 \text{ Wm}^{-2} \text{ K}^{-1}$ in the present study for simplicity [34]. To consider and account for the heat transferred to the surroundings by thermal radiation, Equation (12) is applied.

$$Q_{rad} = \varepsilon_{surf} \sigma A (T_{surf}^4 - T_{surr}^4) \quad (12)$$

where Q_{rad} is the radiation heat-transfer rate, ε_{surf} is the emissivity of the material, σ is Stefan–Boltzmann constant, T_{surf} is the surface temperature, and T_{surr} is the surrounding temperature.

The energy balance for the system along with the heat sink can be written as follows:

$$Q_{heatsink} = G_{total} - Power_{electrical} - Q_{conv} - Q_{rad} \quad (13)$$

The heat extracted by the heat sink $Q_{heatsink}$ is coupled with the ARS model. G_{total} is total received direct radiation on the CPV cell, and $Power_{electrical}$ is the electrical power generated by the CPV cell. At the thermal fluid side, the $Q_{heatsink}$ can be expressed by:

$$Q_{heatsink} = \dot{m} c_p (T_{s,out} - T_{s,in}) \quad (14)$$

The simulations were resolved using the finite element method provided inside COMSOL Multiphysics and the fully coupled solver for applied physics. The following assumptions were used in the simulations:

1. Based on monthly average irradiance data taken from the European Commission PVGIS [35], the direct incoming solar radiation on the Fresnel lens was calculated to be uniform.
2. Germanium material was depicted as a single layer, 0.1 mm thick, that makes up the CPV cell.

3. The heat sink's entrance flow was a fully developed turbulent flow with a velocity of 0.5 m/s. At the exit, atmospheric pressure was considered.
4. Apart from the CPV assembly sections, the heat sink was assumed to be thermally insulated.

The input parameters that were used in COMSOL Multiphysics are listed in Table 2.

Table 2. The input parameters used in the CPV/T model [26,36].

Parameter	Value
The reference efficiency of the CPV Cell (η_{ref})	42%
The optical efficiency (η_{Opt})	92%
The refractive index of Fresnel lens	1.49
The refractive index of exterior domains (air)	1
Heat capacity of water	4200 J·kg ⁻¹ K ⁻¹
The cell-efficiency coefficient ($\beta_{thermal}$)	0.047% K ⁻¹

The dimensions and materials selection of the CPV/T along with the heat sink is listed in Table 3. The arrangement of CPV/T system components is shown in Figure 3.

Table 3. Dimensions of the CPV/T assembly and heat sink [37].

Material	Area	Thickness
Germanium layer	10 mm × 10 mm	0.1 mm
Copper layer	29 mm × 29 mm	0.3 mm
Al ₂ O ₃ layer	30 mm × 30 mm	0.4 mm
Bottom copper layer	29 mm × 29 mm	0.3 mm
Aluminum heat-sink channel (1800 mm length)	30 mm × 10 mm	1.5 mm

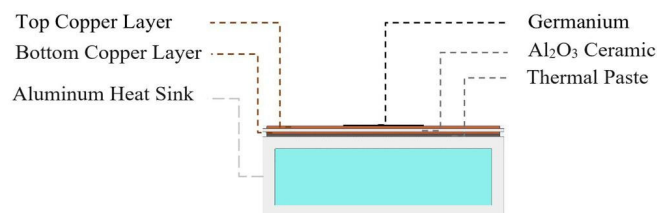


Figure 3. The layers' arrangement in the CPV/T assembly.

Table 4 lists the thermophysical properties of the material utilized in the simulations for the CPV/T model.

Table 4. Thermophysical properties of the components of the CPV/T assembly [38].

Material	Density (kg·m ⁻³)	Heat Capacity (J·kg ⁻¹ ·K ⁻¹)	Thermal Conductivity (W·m ⁻¹ ·K ⁻¹)
Germanium	5323	310	60
Copper	8960	385	400
Al ₂ O ₃ ceramic	3700	880	20
Aluminum	2700	900	170
Thermal paste	4000	800	10
Polymethyl methacrylate	1190	1420	0.19
Cooling water	1000	4200	0.59

2.2. Integration of Refrigeration Subsystems

2.2.1. Adsorption Refrigeration System

The model created by Elsheniti et al. [25] served as the basis for the creation of the ARS model in this study. The detailed pressure-distributed parameter model proposed in [25] was modified in this work to be in the form of a lumped parameter model to make it easier to integrate the ARS model with the thermal outputs of the CPV/T model and to optimize the cycle time of the ARS. Accordingly, a numerical study was conducted in COMSOL Multiphysics by developing a new lumped-parameter model for the system. The ARS utilizes an emerging aluminum-foam bed filled with Maxsorb III adsorbent to make ice using a two-bed configuration system. The evaporator and condenser components of the ARS model were also coupled with zero-dimensional modelling techniques. An ethylene glycol/water mixture that enters the evaporator at $-2\text{ }^{\circ}\text{C}$ was cooled down using the ethanol refrigerant that circulates in the AR system. An ice box was chilled using the mixture that the evaporator cooled. The following is a summary of the governing equations used to model the ARS.

a. Bed model

The energy balance equations for the two beds (b1&b2) take into consideration the application of Al-Foam on the bed tubes and can be written as follows:

$$(M_s C_s + M_s C_{rl} X_{b1} + M_b C_b + M_{foam} C_{foam}) \frac{dT_{b1}}{dt} = (1 - \zeta_{bed}) [\dot{m}_{ca} C_{ca} \varepsilon_{ca} (T_{ca,i} - T_{b1})] - \zeta_{bed} [\dot{m}_h C_h \varepsilon_h (T_{s,out} - T_{b1})] + Q_s M_s \frac{dX_{b1}}{dt} \quad (15)$$

$$(M_s C_s + M_s C_{rl} X_{b2} + M_b C_b + M_{foam} C_{foam}) \frac{dT_{b2}}{dt} = (\zeta_{bed}) [\dot{m}_{ca} C_{ca} \varepsilon_{ca} (T_{ca,i} - T_{b2})] - (1 - \zeta_{bed}) [\dot{m}_h C_h \varepsilon_h (T_{s,out} - T_{b2})] + Q_s M_s \frac{dX_{b2}}{dt} \quad (16)$$

where ζ_{bed} is an operator used in the programming to switch between cooling and heating terms in the equations, providing only cooling/heating effect for bed-1/bed-2 and alternating between them each half of cycle. $M_s C_s$, $M_b C_b$, and $M_{foam} C_{foam}$ are the masses and specific heats of the solid sorbent, bed and foam, respectively. C_{rl} is the specific heat of the adsorbate. The term that includes the amount of adsorbate $M_s X_{b1}$ or $M_s X_{b2}$ is the only time-dependent mass term of the thermal masses of the two beds, since the two beds are identical. \dot{m}_{ca} and \dot{m}_h are the bed cooling and heating water mass flow rates, respectively. Q_s is the heat of adsorption. ε_{ca} and ε_h are the effectiveness of the foam bed during cooling and heating. These heat-transfer parameters depend on the thermal resistance in the foam domain, which is affected by the thermophysical properties of the foam structure and the adsorbent material along with the foam thickness and heating and cooling temperatures and mass flow rates. For simplifications required in the present lumped model, the values of ε_{ca} and ε_h were adapted from the more detailed CFD model used in reference [25] to be 0.802 and 0.853, respectively, and the results were verified for the given case of study.

b. Evaporator model

The evaporator component was simulated using a lumped model that describes the heat balance between the refrigerant and the cooling medium as follows:

$$\left[M_{eva,rl} C_{p,eva,rl} + M_{eva,met} C_{p,eva,met} \right] \frac{dT_{eva}}{dt} = \dot{m}_{Eth,Gly} C_{p,Eth,Gly} \varepsilon_{eva} (T_{Eth,Gly,i} - T_{eva}) - (1 - \zeta_{eva}) [LH_{eva} - C_{p,rl} (T_{cond} - T_{eva})] M_s \frac{dX_{b1}}{dt} - (1 - \psi_{eva}) [LH_{eva} - C_{p,rl} (T_{cond} - T_{eva})] M_s \frac{dX_{b2}}{dt} \quad (17)$$

where $M_{eva,rl} C_{p,eva,rl}$ are the mass and the specific heat of the liquid ethanol in the evaporator. $M_{eva,met} C_{p,eva,met}$ are the mass and the specific heat of metals used in the evaporator component. $\dot{m}_{Eth,Gly}$ is the ethylene glycol mass flow rate. ψ_{eva} & ζ_{eva} are operators that take 0 or 1 values depending on the mode of operation at each switching time to determine the connection with the beds (on/off). M_s is the solid adsorbent mass in each bed. The instantaneous adsorption rate ($\frac{dX_b}{dt}$) is used to calculate the vapor evaporated during the adsorption process in the connected bed. LH_{eva} is the latent heat of evaporation which was calculated based on thermodynamic functions at different evaporation temperatures,

and the term $C_{p,rl}(T_{cond} - T_{eva})$ was used to eliminate the effect of vapor evaporated in the throttling process from the latent heat. The evaporator effectiveness ε_{eva} can be defined using the overall heat-transfer conductance of the evaporator, UA_{eva} , as follows:

$$\varepsilon_{eva} = 1 - \exp\left(\frac{-UA_{eva}}{\dot{m}_{Eth,Gly}C_{p,Eth,Gly}}\right) \quad (18)$$

c. Condenser model

The energy balance equation for the condenser was used to identify the condensing temperature. The cooling water of \dot{m}_{cw} mass flow rate was used to absorb the heat from the condenser. The sensible heat of ethanol vapor per unit mass coming into the condenser ($C_{p,rv}(T_{b2} - T_{cond})$) was added to the condenser latent heat LH_{cond} . It should be remembered that the desorption rate, represented by $\frac{dX_b}{dt}$, is a negative value for the bed connected to the condenser. ψ_{cond} and ζ_{cond} are operators used to mimic the switching process between the two beds in the programming. Therefore, the lumped model for the condenser component can be written as follows:

$$\left[M_{cond,rl} C_{p,cond,rl} + M_{cond,met} C_{p,cond,met} \right] \frac{dT_{cond}}{dt} = \dot{m}_{cw} C_{p,cw} \varepsilon_{cond} (T_{cw,i} - T_{cond}) - (1 - \zeta_{cond}) [LH_{cond} + C_{p,rv}(T_{b1} - T_{cond})] M_s \frac{dX_{b1}}{dt} - (1 - \psi_{cond}) [LH_{cond} + C_{p,rv}(T_{b2} - T_{cond})] M_s \frac{dX_{b2}}{dt}. \quad (19)$$

The condenser effectiveness ε_{cond} can be calculated from Equation (20).

$$\varepsilon_{cond} = 1 - \exp\left(\frac{-UA_{cond}}{\dot{m}_{cw,cond} C_{p,cw}}\right) \quad (20)$$

The liquid phase of refrigerant was considered to have fixed masses and specific heats in both the evaporator and condenser components, while the temperature of liquids varies with time. The liquid refrigerant in the evaporator was at the evaporation temperature, and the liquid phase in the condenser was at the condensing temperature. This is represented by the first term on the LHS of Equations (17) and (19), in addition to the thermal masses of the metals of both components. This approach has been commonly used in modelling the condenser and evaporator of the ARS [39,40].

d. Adsorption isotherms and kinetics

The following set of equations was used to determine the equilibrium adsorption uptake of Maxsorb III/ethanol (X_{eq}) and the instantaneous amount of adsorbate (X) [25,41].

$$X_{eq} = X_{max} \exp\left[-\left(\frac{RT_b}{E} \ln\left(\frac{P_s}{p}\right)\right)^n\right] \quad (21)$$

$$P_s = 0.1333 \times 10^{8.1122 - \frac{1592.864}{T_b + 226.184}} \quad (22)$$

$$\frac{\partial X}{\partial t} = K_{LDF} (X_{eq} - X) \quad (23)$$

$$K_{LDF} = \mathcal{A} \exp\left(\frac{-E_a}{\mathcal{R}_u T_b}\right) \quad (24)$$

where $X_{max} = 1.2 \text{ kg}\cdot\text{kg}^{-1}$, $R = 0.1805 \text{ kJ}\cdot\text{kg}^{-1}\cdot\text{K}^{-1}$, $E = 139.5 \text{ kJ}\cdot\text{kg}^{-1}$, and $n = 1.8$ and denote the maximum uptake, ethanol-gas constant, characteristic energy, and heterogeneity parameter, respectively [42]. P_s and p are saturation pressure at the bed temperature and pressure of the connected evaporator/condenser component, respectively. The linear driving force model was used to define the adsorption/desorption rate, Equation (23). K_{LDF} is the overall intra-particle mass-transfer coefficient, $\mathcal{A} = 132.89 \text{ s}^{-1}$, $E_a = 22.97 \text{ kJ}\cdot\text{mol}^{-1}$, and $\mathcal{R}_u = 8.314 \text{ kJ}\cdot\text{kmol}^{-1}\cdot\text{K}^{-1}$ denote the pre-exponential constant, activation energy, and universal gas constant, respectively [41].

e. Adsorption-system coupling and performance indicators

The hybrid system's configuration settings were all set to fixed values. At the given regeneration temperature, the available amount of regeneration energy will fluctuate each month. Varying the cycle time of the adsorption system is an option proposed in the present study. This option was utilized to match the outputs of the CPV/T system with the heating load required by the ARS. The adsorption system was working under transient conditions. Therefore, numerical integration was used to average the outputs and calculate the system performance based on the average performance of the day, as follows:

$$Q_{heat,ads} = \frac{1}{t_{cycle}} \int_0^{t_{cycle}} \dot{m}_{hw} C_{hw} (T_{hw,i} - T_{hw,out}) dt \quad (25)$$

where $Q_{heat,ads}$ should be the average regeneration heat provided by the CPV/T system at a given month by adapting the cycle time, and the heating temperature is equal to the outlet temperature from the CPV/T system ($T_{hw,i} = T_{s,out}$). The average cooling capacity of the adsorption system ($Q_{eva,ads}$) can be computed as follows:

$$Q_{eva,ads} = \frac{1}{t_{cycle}} \int_0^{t_{cycle}} \dot{m}_{Eth,Gly} C_{Eth,Gly} (T_{Eth,Gly,i} - T_{Eth,Gly,out}) dt \quad (26)$$

The average (COP_{ads}), the average specific cooling power (SCP_{ads}), and the daily ice production (DIP_{ads}) are calculated as follows:

$$COP_{ads} = \frac{Q_{eva,ads}}{Q_{heat,ads}} \quad (27)$$

$$SCP_{ads} = \frac{Q_{eva,ads}}{M_S} \quad (28)$$

$$DIP_{ads} = \frac{Q_{eva,ads} * 3600 * Working\ hours}{C_{p,w} (T_{w,in} - T_{freezing}) + h_{fg} + C_{p,ice} (T_{freezing} - T_{ice,out})} \quad (29)$$

where $T_{w,in}$ is assumed to be variable and set according to the ambient temperature for each month, and $T_{freezing}$ is the freezing temperature of water. The main parameters used for the beds in simulation are listed in the Table 5, while Table 6 shows the parameters used for the condenser and evaporator.

Table 5. Main parameters used in the simulation for the foamed beds [25].

Parameter	Value	Unit
Activated-carbon density (ρ_s)	2200	kg·m ⁻³
Activated-carbon specific heat ($C_{p,s}$)	1375	J·kg ⁻¹ ·k ⁻¹
Aluminum-foam density (ρ_{fo})	270	kg·m ⁻³
Aluminum-foam specific heat ($C_{p,fo}$)	895	J·kg ⁻¹ ·k ⁻¹
Bulk density (ρ_{bulk})	2775	kg·m ⁻³
The geometrical and operating parameters of the beds		
Adsorbent mass for each bed	1.25	kg
Heating-water mass flowrate (\dot{m}_{hw})	5.394	kg·s ⁻¹
Cooling-water mass flowrate ($\dot{m}_{cw,b}$)	2.543	kg·s ⁻¹
Inlet cooling-water temperature ($T_{cw,i}$)	25	°C
Tube length	0.4	m
Tube inner radius	3.15	mm
Tube outer radius	3.96	mm
Aluminum-foam thickness	2	mm
Number of tubes	100	–

Table 6. Condenser and evaporator parameters [43].

Symbols	Value	Unit
$M_{cond,rl} C_{p,cond,rl} + M_{cond,met} C_{p,cond,met}$	$2.5 \times 3064 + 12 \times 368$	$J \cdot K^{-1}$
UA_{cond}	4114×1.855	$W \cdot K^{-1}$
$\dot{m}_{cw} C_{p,cw}$	0.6271×4180	$W \cdot K^{-1}$
$T_{cw} C_{p,cw}$	25	$^{\circ}C$
$M_{eva,rl} C_{p,eva,rl} + M_{eva,met} C_{p,eva,met}$	$20 \times 2251 + 4.45 \times 386$	$J \cdot K^{-1}$
UA_{eva}	2557×0.6	$W \cdot K^{-1}$
$\dot{m}_{Eth,Gly} C_{p,Eth,Gly}$	0.424×3574.3	$W \cdot K^{-1}$
$T_{Eth,Gly,out}$	-2	$^{\circ}C$

2.2.2. Vapor Compression System

Given the electrical output of the CPV/T system and the higher anticipated ambient temperature, we decided to choose an off-the-shelf VCS. Table 7 shows the main parameters of the chosen system, namely, Copeland XHV0181P [44].

Table 7. Vapor compression system parameters [44].

Parameter	Value	Unit
Power input	0.9–3.7	kW
Cooling capacity ($Q_{eva,vc}$)	2.6–11.3	kW
Condensing temperature	50	$^{\circ}C$
Evaporating temperature	-5	$^{\circ}C$
COP	2.89–3.05	-
Refrigerant	R410a	-

The daily ice production of the VCS (DIP_{vc}) was calculated by:

$$DIP_{vc} = \frac{Q_{eva,vc} * 3600 * Working\ hours}{C_{p,w} (T_{w,in} - T_{freezing}) + h_{fg} + C_{p,ice} (T_{freezing} - T_{ice,out})} \quad (30)$$

where $Q_{eva,vc}$ is obtained from the compressor datasheet and is based on the given power and the operating conditions.

3. Results and Discussions

3.1. Validation of the CPV/T Simulation Model

The developed thermal model for the CPV/T is compared and validated against two experimental studies. The first is a validation with the study conducted by Aldossary et al. [45], where an electrical resistance heater was used to simulate the heat load applied to the CPV cell. The surface average temperature of the cell was around $52.15^{\circ}C$. The simulation performed by Aldossary for the model indicated a maximum cell temperature of $55^{\circ}C$ compared to $57^{\circ}C$ for the current developed model. The comparison of the experimental results and the current thermal model shows close agreement at several selected points, as depicted in Figure 4. The temperature at the top of the CPV assembly from the experimental works is approximately 8% higher than the thermal model. However, for other points such as the coolant outlet, sides of the heat sink, and top of the heat sink, temperatures range between 0.5% for the side surfaces and around 3% for the water outlet and top of the heat sink.

To confirm the validity of the present CPV/T model under the inputs of the outdoor dynamic conditions, the present model results were validated with the experimental results of Wu et al. [46]. They performed an outdoor experimental evaluation for a CPV cell utilizing a heat sink with double bifurcation channels. The test was performed at 500X

solar concentration and a water flow rate at 28.7 mL/min and inlet temperature of 30 °C. The experiment was conducted from 10:30 to 14:30 during the summer season. The study showed that the maximum average temperature achieved at 12:00 was around 71 °C. This agrees with the developed thermal model, which achieved an average temperature of 70.3 °C on the CPV cell surface under the same transient conditions using the current developed model.

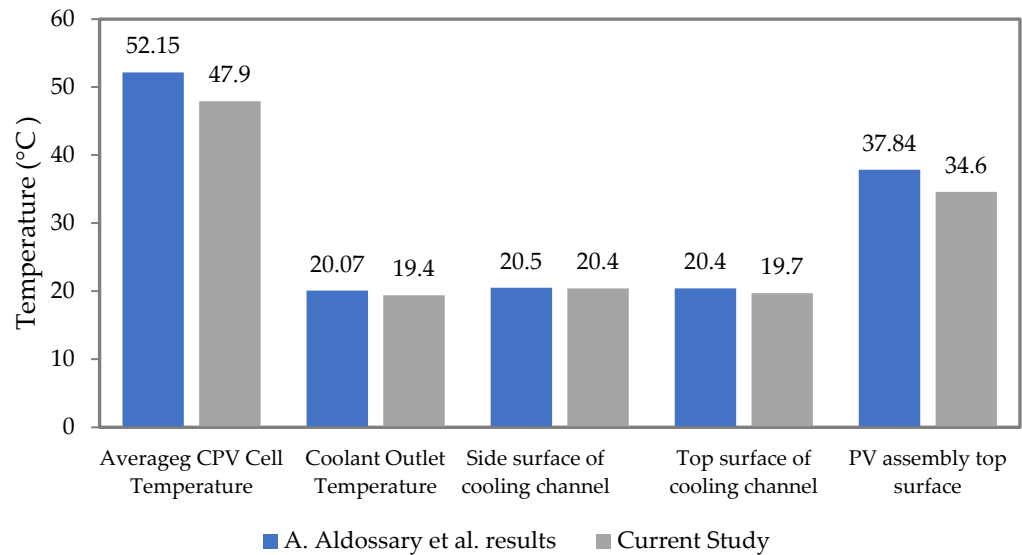


Figure 4. The validation of the CPV/T numerical model with reference [45].

3.2. Thermal and Electrical Outputs of the CPV/T System

The thermal model simulation was carried out as per the previous sections’ assumptions and methodology. The simulation was run based on the weather data of the city of Riyadh for a full year; therefore, the ambient and normal irradiance varied accordingly. Figure 5 shows the variations in the direct solar irradiance and ambient temperature over the daylight of each month in Riyadh city [35]. Figure 6 shows the average daily total direct irradiance received in each month.

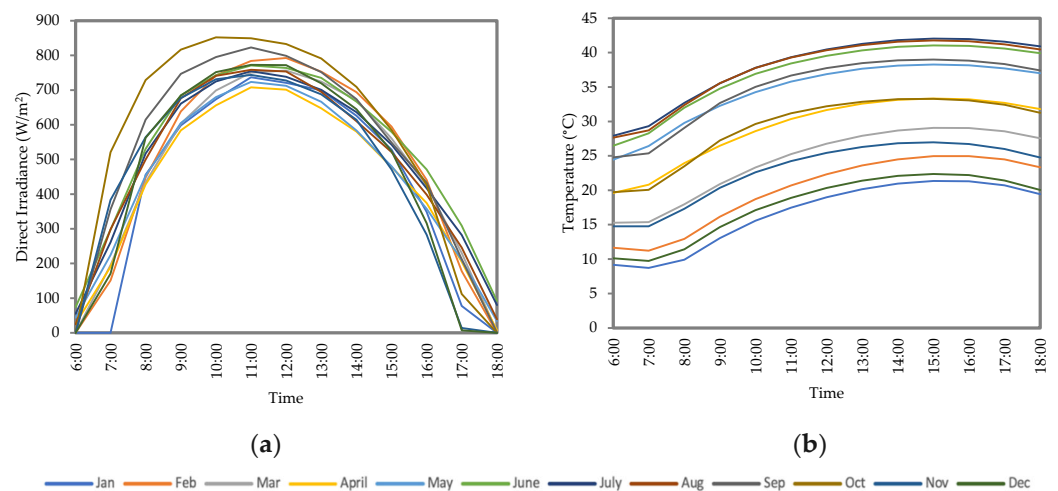


Figure 5. Solar radiation and ambient temperature profiles of a representative day of each month: (a) solar irradiance and (b) ambient temperature.

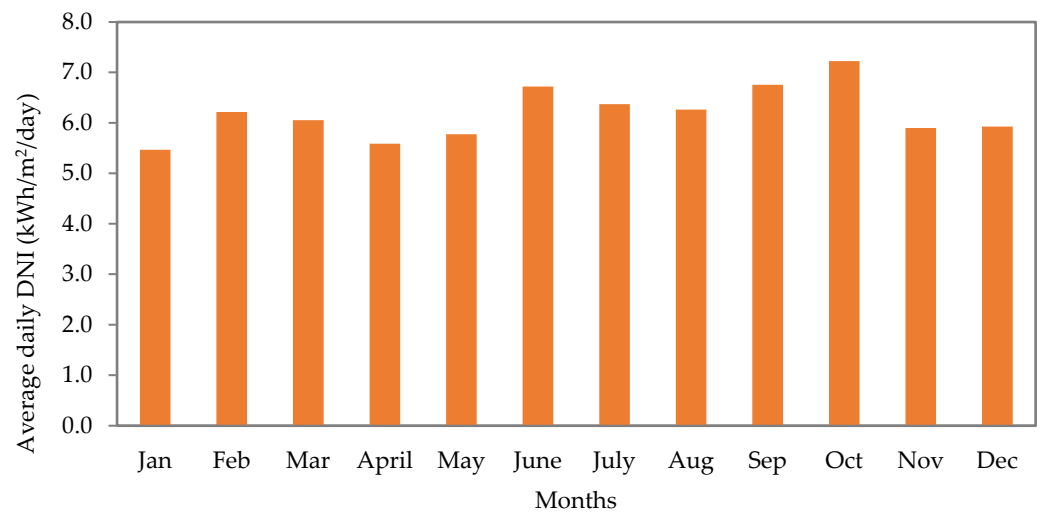


Figure 6. Average DNI distribution.

A mesh sensitivity analysis was conducted for the study to compare the difference in the coolant temperatures versus the mesh elements. The analysis showed that the difference between the inlet and outlet temperatures was converging after 1.76 million elements with an error percentage of less than 0.5%, as illustrated in Figure 7.

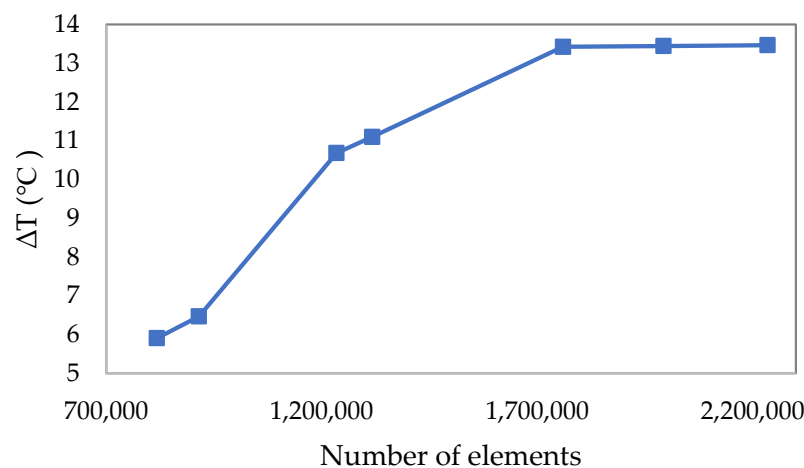


Figure 7. Mesh sensitivity analysis.

Since the ARS requires an outlet temperature of 90 °C from the CPV/T, multiple CPV cell were connected in series in order to achieve the required temperature. According to the simulation model, a minimum of four CPV cells were needed to achieve a temperature of approximately 90 °C. Concurrently, it was confirmed that the maximum operating temperature of the CPV cell did not exceed 110 °C [17]. The simulation confirmed that the maximum operating temperature of the cells was acceptable when four CPV cells were connected in series with an inlet flow temperature of 89.75 °C and at a flow rate of 5.67 L·min⁻¹. Even though the cell temperature was higher than 80 °C, the thermal energy obtained from the system was highly beneficial for the integrated refrigeration system. The extracted thermal energy from the fluid was used for the ARS, which operates in such ranges at a higher performance [25,47].

Due to the high inlet water temperature, the cell-surface temperatures were about 100.14 °C, as shown in Figure 8. Based on that, the cell efficiency was lower than the optimal efficiency of 42% and was around 37–38%.

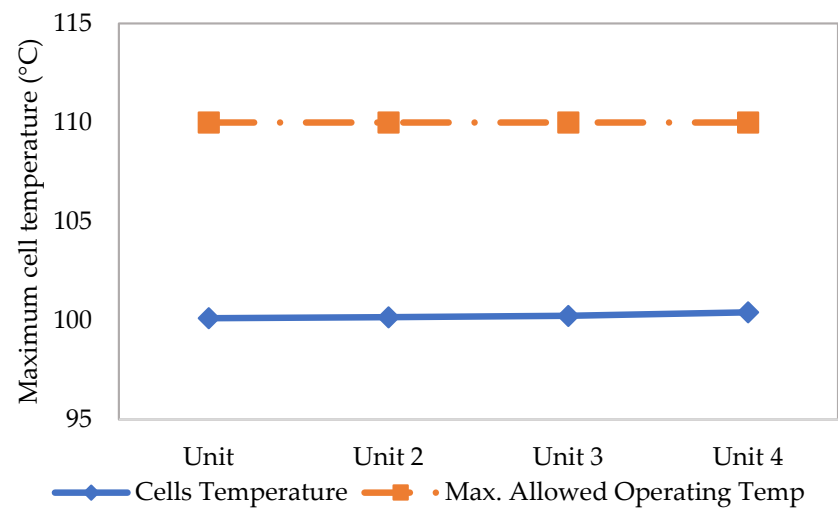


Figure 8. Cell maximum temperature at each unit over the cooling channel.

The temperature profile for the CPV/T assembly for one row is shown in Figure 9. The system consists of four CPV cells in series, where the NDI is uniformly distributed on the cells. The simulation took into account the water's input temperature of 89.75 °C and flow rate of 5.67 L·min⁻¹.

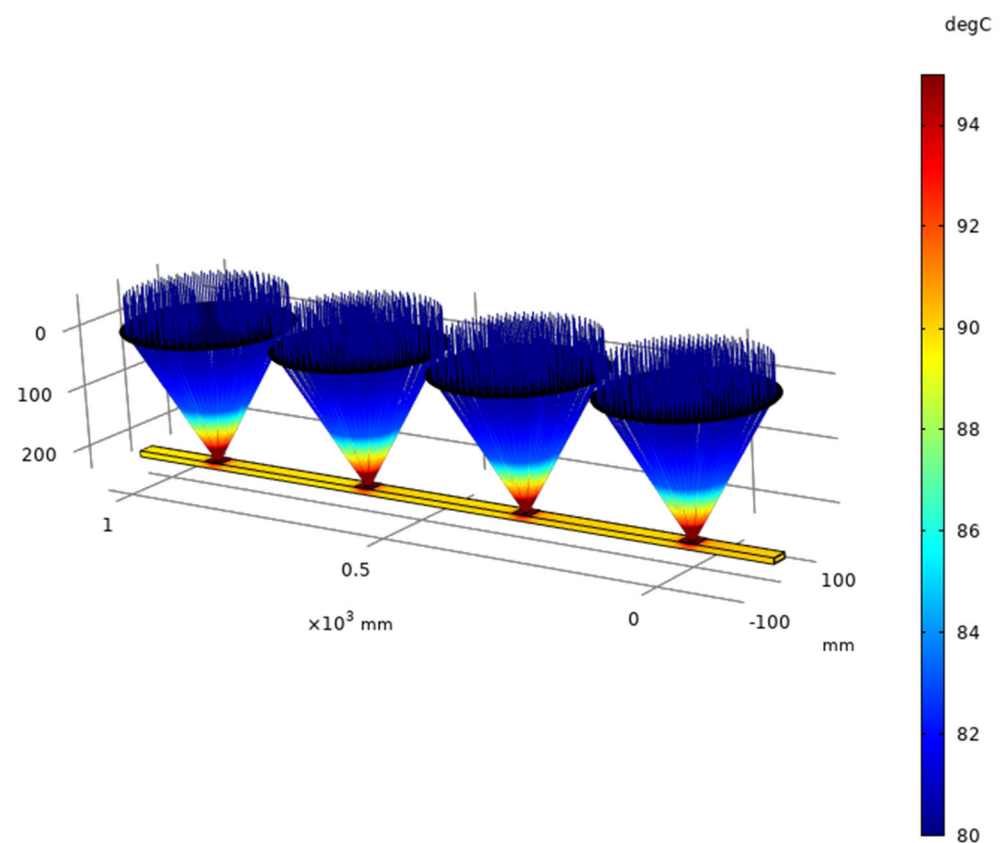


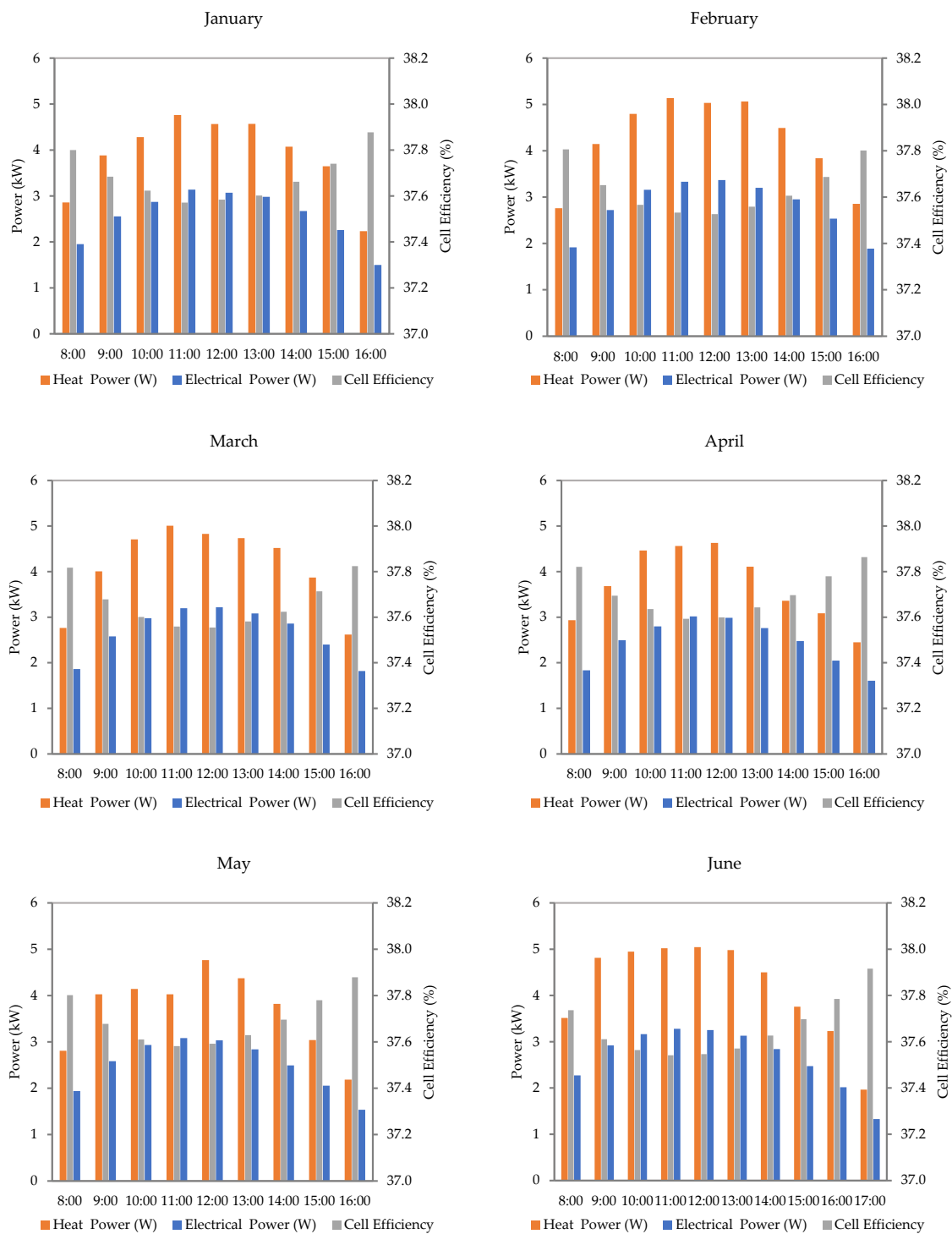
Figure 9. Temperature profile for the CPV/T assembly.

The thermal power generated by the assembly was calculated using Equation (15) for each given condition. Based on that, the assembly with four CPV cells in series produced approximately from 0.574 to 0.722 kWh electrical energy on average per day, and it varied based on the ambient conditions. The operating hours were 9 or 10 h. This was calculated using a 500X solar concentration and a water inflow moving at 0.5 m/s. As a result, in order to operate the adsorption refrigeration system, many sets of assemblies must be connected in parallel in order to provide the system with the necessary thermal energy in terms of temperature level and flow rate. In the event that an outlet temperature at a higher level is required, additional cells must be added to the assembly and connected in series.

The convective heat transmission from the heat sink walls is a crucial factor that needs to be taken into account. The majority of heat losses from the heat sink to the environment are caused by convection heat transfer. Ignoring these losses could result in a 25% reduction in the thermal energy produced. In order to ensure that less energy be lost to the environment, insulation must be applied to the heat sink. The heat sink in the presented model was insulated except at the CPV assembly, where some heat was lost due to radiation and convection heat transfer to the ambient. With those assumptions, the CPV/T system achieved an overall efficiency of 86.4%. Based on the simulation results and the required mass flow rate for the adsorption system, a total of 58 assemblies, each combining four CPV/T, needs to be connected in parallel to operate the ARS. The whole system was evaluated for the whole year using recorded weather data in Riyadh [28]. The monthly performance of the CPV/T system is depicted in Figure 10a,b. This figure shows the variation in the heat and electrical power outputs and cell electrical efficiency over the representative day of each month from 8:00 to 16:00, which extends to 17:00 in the months from June to August. The output heat power from the system considers the heat losses from the CPV assembly, and the electrical power output is directly from the CPV cells. Overall, the electrical and heat powers attained their maximum values at about 10:00 to 11:00, affected by the highest DNI. The maximum electrical and heat powers were 3.62 kW and 5.62 kW, respectively, in October at 10:00. However, the cell temperatures were the highest at these times, preventing the cell electrical efficiencies from becoming higher at these times.

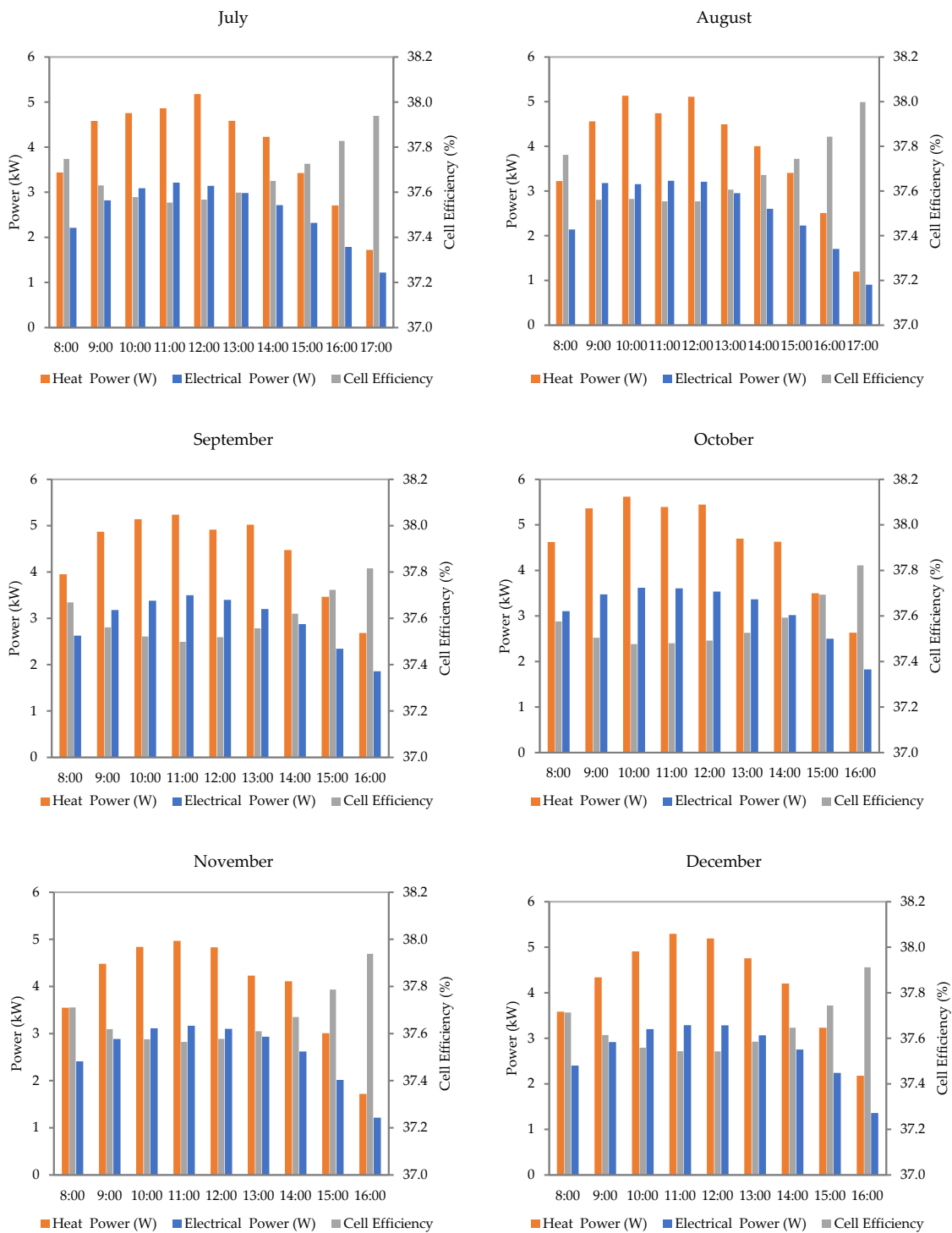
The daily average energy generated from the CPV/T system each month is summarized in Figure 11. It can be deduced that the system generated a daily electrical energy of 28.0 kWh on average in October, which represented the maximum daily electrical-energy amount over the year, while the corresponding minimum value of 22.0 kWh was in April. The associated daily average thermal energy provided by the CPV/T system ranged from 41.9 kWh in October to 33.2 kWh in April and May.

In general, a storage system is required, as with any solar-powered system, to smooth out output swings. Consequently, the CPV/T needs to have electrical and thermal storage systems. On average throughout the year, the CPV/T system may produce 24.7 kWh of electrical energy daily and 37.6 kWh of thermal energy.



(a)

Figure 10. Cont.



(b)

Figure 10. (a) Daily average thermal and electrical power production for months from January to June. (b) Daily average thermal and electrical power production for months from July to December.

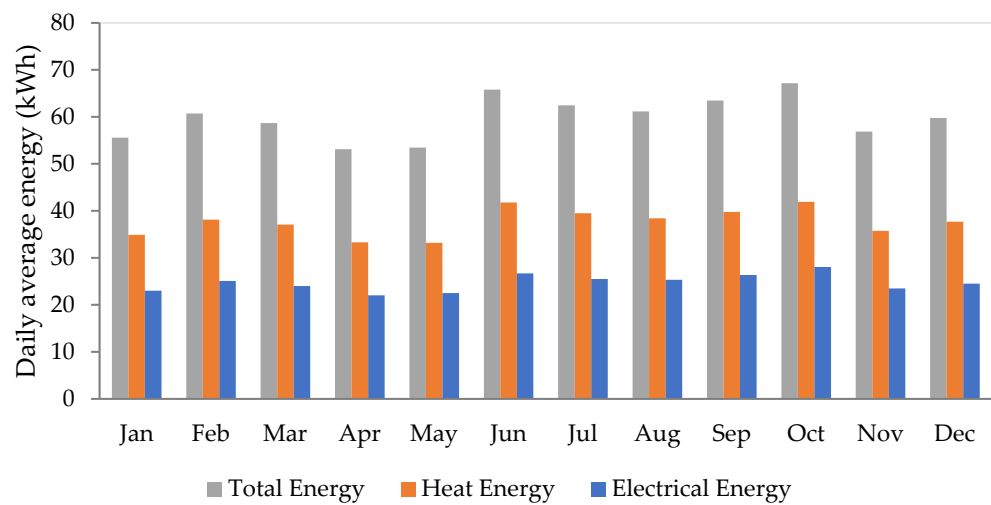


Figure 11. Average daily energy generation for each month in Riyadh.

3.3. Daily Ice Production of the Integrated System

This section discusses the results of the two refrigeration systems, which are driven by the average daily outputs of the CPV/T system, considering the use of energy storage systems. The physical and operating parameters of the adsorption system were adopted to match the available heat power and provide the best performance in light of the results of the previous investigations. Therefore, a 2 mm foam thickness was chosen as recommended in reference [25] for a similar application. The feed water for the regeneration was $5.394 \text{ kg}\cdot\text{s}^{-1}$ at 90°C during working hours. The heat recovered from the CPV/T system was incorporated into the developed lumped model, and the simulation was performed by taking the daily average thermal power for each month, which ranged between 3.7–4.7 kW.

The results of the constructed ARS model used in this study and information from earlier studies indicate that extending the cycle duration improves the ARS's COP since less thermal power is required. By adjusting the cycle time throughout the year, this behavior of the ARS with the cycle time was used to aid the optimal integration with the CPV/T system. Figure 12 shows the optimum cycle times selected for each month, which ranged from 900 to 1160 s. It can be noticed that the months with lower thermal power required a higher cycle time for the best combination with the CPV/T outputs. The figure shows that the SCP attained its best value of $487 \text{ W}\cdot\text{kg}^{-1}$ in October, associated with the lower cycle time of 900 s, while the minimum SCP of $377.5 \text{ W}\cdot\text{kg}^{-1}$ in April was reached using the higher cycle time of 1160 s.

The performance of the VCS was based on the electrical output of the CPV/T system, which ranged from 0.9 to 3.25 kW depending on the operational conditions. A variable-speed compressor from the manufacturer Copeland was selected with a minimum electrical input of 0.9 kW and a maximum of 3.7 kW [44]. This made it possible to operate the VCS using alternative CPV/T system electrical outputs. It is important to highlight that the electrical power consumption needed by the auxiliary systems of the integrated assembly was considered in the final evaluation, such as the losses in the inverter which is typically coupled with the solar PV.

Figure 13 shows the monthly average daily output of ice that can be made by both refrigeration systems in the city of Riyadh over the course of a year. Over the course of the year, the VCS and the ARS generated DIP at rates of 417.7 kg per day and 76.7 kg per day, respectively. The months of October and May generated the highest and lowest daily averages of total DIP, 572.9 kg and 416.7 kg, respectively. This was attributable to the levels of ambient temperature and the amount of direct irradiance during these two months. A solar COP of 0.875 was achieved for the integrated system's energy conversion efficiency on average over the course of the year, which is a promising result when compared to earlier research [11,48].

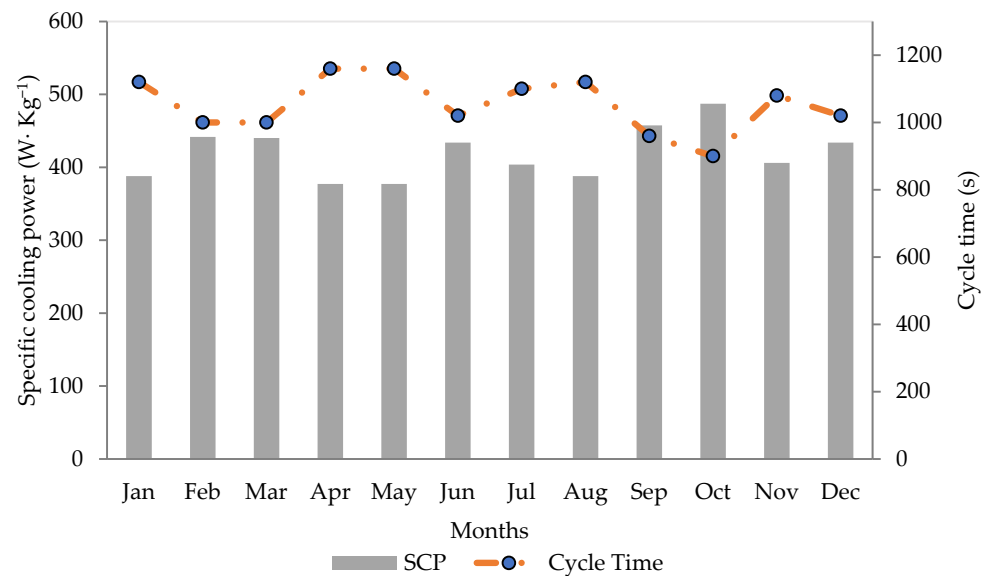


Figure 12. Optimum cycle time and the corresponding SCP of the ARS for each month.

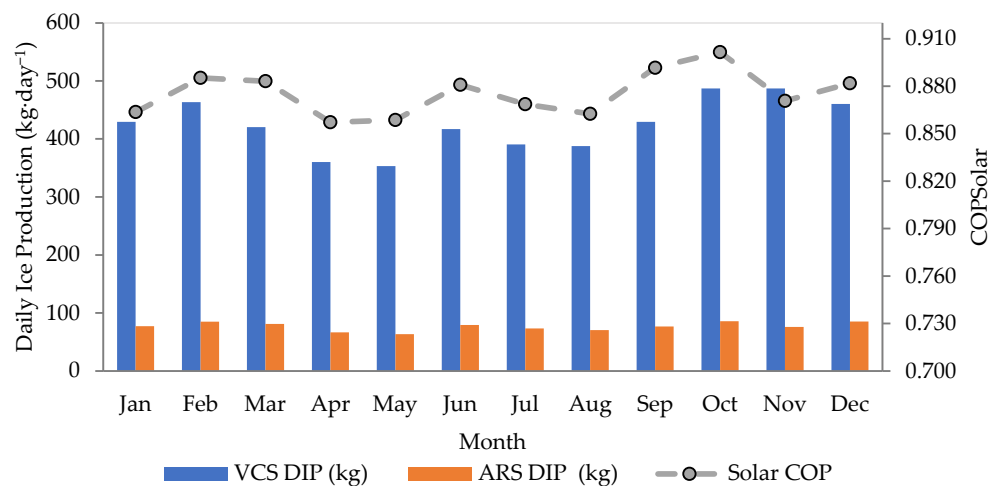


Figure 13. Average daily ice production of each month in Riyadh from the VRS and ARS.

3.4. Energy Balance Sheet

An energy balance sheet was created for a selected case on an average day in October to assess the proposed hybrid solar ice-production system discussed in the present study. The energy assessment in the balance sheet shows the power consumption of the auxiliary systems and the power losses that are typically associated with the operation of such a system, including:

- Optical solar losses from the Fresnel lens.
- Inverter losses.
- Thermal losses from CPV assembly surfaces.
- VCS electrical losses.
- ARS losses.

The available DNI on the proposed CPV/T system was approximately 9 kW on average during the operating hours of October, in Riyadh, considering the CPV/T assembly covered an area of approximately 12.5 m² as the facing area of Fresnel lenses. The generated electrical power was converted to AC through a 90% efficient inverter and distributed between the VCS and the auxiliary systems. It was assumed that the auxiliary systems consumed 0.5 kW and the remaining 2.3 kW was used to power the VCS. An additional

electrical power of 0.32 kW was used for the associated components of the VCS, such as the condenser fan. The heat losses from the CPV/T assembly, connections, piping, and other fittings were assumed to be 0.5 kW.

Figure 14 illustrates the energy balance chart for the integrated solar-driven refrigeration system and outlines the system's performance. According to the given conditions and assumptions, the combined cooling capacity of the hybrid system was around 8.1 kW, which resulted in a daily ice production of approximately 572.9 kg. Due to its higher COP than the ARS, the VCS contributed to the production of ice to an extent of roughly 85%. An excellent opportunity to implement such a system in Riyadh and similar locations is provided by the anticipated standalone CPV/T system's overall solar COP of 0.9, which can be achieved in October. In actuality, the operational circumstances of the hybrid system can be efficiently optimized by adapting an appropriate control system [49]. The present study's findings can be used to identify the necessary control strategies.

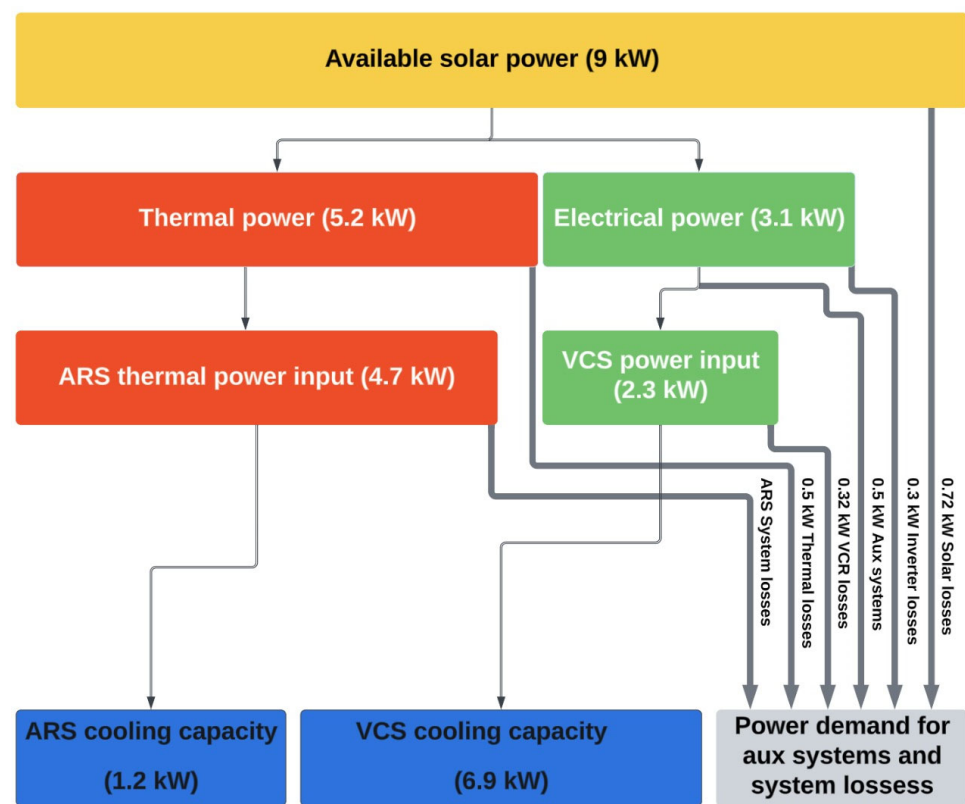


Figure 14. Power distribution chart for the integrated system.

4. Conclusions

The current study proposed and mathematically investigated a combined solar CPV/T system that drives two refrigeration systems, a vapor compression type and an adsorption type, to produce ice under Riyadh weather conditions. To make the best utilization of the available input power, matching the time variations of the solar-power intensity was accomplished in this study by choosing a variable-speed compressor for the VCS and optimizing the cycle time of the ARS. In addition, the integrated system power losses and power demand for the auxiliary systems were considered in evaluating the performance of the overall system. The following were the main outcomes:

- The integrated system managed to achieve a maximum DIP of about $573 \text{ kg} \cdot \text{day}^{-1}$, on average, in October, while the minimum DIP was in May of $416.7 \text{ kg} \cdot \text{day}^{-1}$, affected by the low DNI along with higher ambient temperature in May compared to April.
- The VCS contributed to about 84.5% of the total ice production over the year, utilized from its higher COP compared to the ARS.

- The average solar COP of 0.875 was attained using the proposed hybrid ice-production system.
- The solar ice maker suggested in this study can replace intermittent solar cooling systems, which produce chilled water, by providing cooling both during the day and at night using the cooling power stored in the ice.

Author Contributions: Conceptualization, M.B.E.; Methodology, M.B.E., H.A.-A., Z.A. and J.O.; Software, M.B.E. and A.A.; Validation, A.A. and Z.A.; Formal analysis, M.B.E. and Z.A.; Investigation, M.B.E. and A.A.; Resources, H.A.-A., J.O. and A.E.-L.; Data curation, A.A. and A.E.-L.; Writing—original draft, M.B.E. and A.A.; Writing—review & editing, M.B.E. and H.A.-A.; Visualization, Z.A., J.O. and A.E.-L.; Supervision, M.B.E. and H.A.-A.; Project administration, H.A.-A.; Funding acquisition, H.A.-A. All authors have read and agreed to the published version of the manuscript.

Funding: This Project was funded by the National Plan for Science, Technology and Innovation (MAARIFAH), King Abdulaziz City for Science and Technology, Kingdom of Saudi Arabia, Award Number (II-ENE1845-02).

Institutional Review Board Statement: Not applicable.

Informed Consent Statement: Not applicable.

Data Availability Statement: The data that support the findings of this study are available from the corresponding author, [M.B.E.], upon reasonable request.

Conflicts of Interest: The authors declare no conflict of interest.

Nomenclature

A	Area (m^2)
A	Pre-exponential factor (s^{-1})
C	Specific heat ($\text{J} \cdot \text{kg}^{-1} \cdot \text{K}^{-1}$)
CR	Concentration ratio
E_a	Activation energy of surface diffusion ($\text{J} \cdot \text{mol}^{-1}$)
f	Focal length (mm)
h	Convective heat transfer coefficient ($\text{W} \cdot \text{m}^{-2} \cdot \text{K}^{-1}$)
k	3D ray vector
K_{cond}	Thermal conductivity of the material ($\text{W} \cdot \text{m}^{-1} \cdot \text{K}^{-1}$)
K_{LDF}	Overall intra-particle mass transfer coefficient (s^{-1})
LH	Latent heat ($\text{J} \cdot \text{kg}^{-1}$)
M	Mass (kg)
\dot{m}	Mass flow rate ($\text{kg} \cdot \text{s}^{-1}$)
n	Refractive index (-)
P_s	Saturation pressure (Pa)
p	Pressure (Pa)
Q_{conv}	Convective heat (W)
$Q_{heatsink}$	Heat extracted by the heat sink (W)
Q_{rad}	Radiation heat (W)
Q_s	Adsorption heat ($\text{J} \cdot \text{kg}^{-1}$)
q_{cond}	Conduction heat transfer ($\text{W} \cdot \text{m}^{-2}$)
q_{heat}	Input energy converted to heat ($\text{W} \cdot \text{m}^{-2}$)
q_{rad}	Solar radiations ($\text{W} \cdot \text{m}^{-2}$)
R	Distance between incident light and the optical axis (m)
\mathcal{R}_u	Universal gas constant ($\text{J} \cdot \text{mol}^{-1} \cdot \text{K}^{-1}$)
T	Temperature ($^{\circ}\text{C}$)
t	Time (s)
UA	Heat transfer conductance ($\text{W} \cdot \text{K}^{-1}$)
X	Uptake ($\text{kg}_{\text{ref}} \cdot \text{kg}_{\text{ad}}^{-1}$)

X_{eq}	Equilibrium adsorption uptake ($\text{kg}_{\text{ref}} \cdot \text{kg}_{\text{ad}}^{-1}$)
X_{max}	Maximum adsorption uptake ($\text{kg}_{\text{ref}} \cdot \text{kg}_{\text{ad}}^{-1}$)
Greek Symbols:	
ε_{surf}	Emissivity of the material (-)
ε_{eva}	The evaporator effectiveness (-)
ε_{cond}	The condenser effectiveness (-)
$\beta_{thermal}$	Cell-efficiency coefficient ($\% \cdot \text{K}^{-1}$)
η_{CPV}	Cell efficiency (%)
η_{Opt}	Optical efficiency (%)
η_{ref}	Reference cell efficiency at 25 °C
α	Prism angle (rad)
ζ_{bed}	An operator used for the programming of Equations (15) and (16) (-)
ε	Effectiveness (-)
θ	The angle between the refractive ray and the perpendicular direction to the prism Surface (rad)
σ	Stefan–Boltzmann constant ($\text{W} \cdot \text{m}^{-2} \cdot \text{K}^{-4}$)
ω	Angular frequency (rad s^{-1})
Subscripts and superscripts:	
ads	Adsorption refrigeration
amp	Ambient temperature
b1	First bed
b2	Second bed
bed	Adsorption bed
ca	Cooling water to adsorber
cond	Condenser
cw	Cooling water
Eth,Gly	Ethylene Glycol
eva	Evaporator
foam	Al foam on bed tubes
h	Hot water
hw	Heating water
i	Inlet
met	Metal
out	Outlet
rl	Refrigerant liquid
rv	Refrigerant vapor
s	Sorption material
s,in	Heat-sink fluid inlet
s,out	Heat-sink fluid outlet
surf	Surface temperature
surr	Surrounding
vc	Vapor compression refrigeration
w	Water
Abbreviations:	
v	Adsorption refrigeration system
COP	Coefficient of performance
CPV	Concentrated photovoltaic
CPV/T	Concentrated photovoltaic thermal
DIP	Daily ice production ($\text{kg} \cdot \text{day}^{-1}$)
DNI	Direct normal irradiance
GCR	Geometrical concentration ratio
MJSC	Multi-junction solar cells
PFFL	Point-focus Fresnel lens
PMMA	Polymethyl methacrylate
SCP	Specific cooling power ($\text{W} \cdot \text{kg}^{-1}$)
VCS	Vapor compression refrigeration system

References

- Almasoud, A.H.; Gandayh, H.M. Future of solar energy in Saudi Arabia. *J. King Saud Univ. Eng. Sci.* **2015**, *27*, 153–157. [CrossRef]
- Alawaji, S.H. Evaluation of solar energy research and its applications in Saudi Arabia—20 years of experience. *Renew. Sustain. Energy Rev.* **2001**, *5*, 59–77. [CrossRef]
- Asif, M. Growth and sustainability trends in the buildings sector in the GCC region with particular reference to the KSA and UAE. *Renew. Sustain. Energy Rev.* **2016**, *55*, 1267–1273. [CrossRef]
- KAPSARC. *The Future of Cooling in Saudi Arabia: Technology, Market and Policy Options*; King Abdullah Petroleum Studies and Research Center: Riyadh, Saudi Arabia, 2020.
- Wang, R.Z.; Pan, Q.W.; Xu, Z.Y. 12—Solar-powered adsorption cooling systems. In *Advances in Solar Heating and Cooling*; Wang, R.Z., Ge, T.S., Eds.; Woodhead Publishing: Sawston, UK, 2016; pp. 299–328.
- Kumar, A.; Kapilan, N.; Dinesh, P.A.; Kasthuriangan, S. Experimental studies on solar assisted activated carbon based adsorption refrigeration system. *Mater. Today Proc.* **2022**, *62*, 5258–5265. [CrossRef]
- Kılıç, M. Evaluation of Combined Thermal–Mechanical Compression Systems: A Review for Energy Efficient Sustainable Cooling. *Sustainability* **2022**, *14*, 13724. [CrossRef]
- Attalla, M.; Sadek, S.; Ahmed, M.S.; Shafie, I.M.; Hassan, M. Experimental study of solar powered ice maker using adsorption pair of activated carbon and methanol. *Appl. Therm. Eng.* **2018**, *141*, 877–886. [CrossRef]
- Luo, H.; Dai, Y.; Wang, R.; Tang, R.; Li, M. Year round test of a solar adsorption ice maker in Kunming, China. *Energy Convers. Manag.* **2005**, *46*, 2032–2041. [CrossRef]
- Wang, Y.; Li, M.; Ji, X.; Yu, Q.; Li, G.; Ma, X. Experimental study of the effect of enhanced mass transfer on the performance improvement of a solar-driven adsorption refrigeration system. *Appl. Energy* **2018**, *224*, 417–425. [CrossRef]
- Ambarita, H.; Kawai, H. Experimental study on solar-powered adsorption refrigeration cycle with activated alumina and activated carbon as adsorbent. *Case Stud. Therm. Eng.* **2016**, *7*, 36–46. [CrossRef]
- Elsheniti, M.B.; Rezk, A.; Shaaban, M.; Roshdy, M.; Nagib, Y.M.; Elsamni, O.A.; Saha, B.B. Performance of a solar adsorption cooling and desalination system using aluminum fumarate and silica gel. *Appl. Therm. Eng.* **2021**, *194*, 117116. [CrossRef]
- Shaaban, M.; Elsheniti, M.B.; Rezk, A.; Elhelw, M.; Elsamni, O.A. Performance investigation of adsorption cooling and desalination systems employing thermally enhanced copper foamed bed coated with SAPO-34 and CPO-27(Ni). *Appl. Therm. Eng.* **2022**, *205*, 118056. [CrossRef]
- Gado, M.; Megahed, T.; Ookawara, S.; Nada, S.; Hassan, H. Performance assessment of photovoltaic/thermal (PVT) hybrid adsorption-vapor compression refrigeration system. *J. Energy Syst.* **2022**, *6*, 209–220. [CrossRef]
- Aghakhani, S.; Afrand, M. Experimental study of the effect of simultaneous application of the air- and water-cooled flow on efficiency in a Photovoltaic thermal solar collector with porous plates. *Appl. Therm. Eng.* **2022**, *217*, 119161. [CrossRef]
- Ju, X.; Xu, C.; Han, X.; Du, X.; Wei, G.; Yang, Y. A review of the concentrated photovoltaic/thermal (CPVT) hybrid solar systems based on the spectral beam splitting technology. *Appl. Energy* **2017**, *187*, 534–563. [CrossRef]
- Ju, X.; Xu, C.; Liao, Z.; Du, X.; Wei, G.; Wang, Z.; Yang, Y. A review of concentrated photovoltaic-thermal (CPVT) hybrid solar systems with waste heat recovery (WHR). *Sci. Bull.* **2017**, *62*, 1388–1426. [CrossRef]
- De Pascale, A.; Ferrari, C.; Melino, F.; Morini, M.; Pinelli, M. Integration between a thermophotovoltaic generator and an Organic Rankine Cycle. *Appl. Energy* **2012**, *97*, 695–703. [CrossRef]
- Albaik, I.; Alamri, Y.A.; Elsheniti, M.B.; Al-Dadah, R.; Mahmoud, S.; Ismail, M.A. Assessment of a novel multi-generation solar CPV/T system combining adsorption and organic rankine cycle subsystems. *Sol. Energy* **2022**, *236*, 455–472. [CrossRef]
- Lin, L.; Tian, Y.; Luo, Y.; Chen, C.; Jiang, L. A novel solar system integrating concentrating photovoltaic thermal collectors and variable effect absorption chiller for flexible co-generation of electricity and cooling. *Energy Convers. Manag.* **2020**, *206*, 112506. [CrossRef]
- Kasaean, A.; Nouri, G.; Ranjbaran, P.; Wen, D. Solar collectors and photovoltaics as combined heat and power systems: A critical review. *Energy Convers. Manag.* **2018**, *156*, 688–705. [CrossRef]
- Xu, Z.; Kleinstreuer, C. Concentration photovoltaic–thermal energy co-generation system using nanofluids for cooling and heating. *Energy Convers. Manag.* **2014**, *87*, 504–512. [CrossRef]
- Alamri, Y.A.; Albaik, I.; Mahmoud, S.; Al-Dadah, R.; Ismail, M.A. Integration of concentrated multi-junction solar cells with small-scale organic rankine cycle. *Energy Convers. Manag.* **2021**, *239*, 114235. [CrossRef]
- Buonomano, A.; Calise, F.; Palombo, A. Solar heating and cooling systems by absorption and adsorption chillers driven by stationary and concentrating photovoltaic/thermal solar collectors: Modelling and simulation. *Renew. Sustain. Energy Rev.* **2018**, *82*, 1874–1908. [CrossRef]
- Elsheniti, M.B.; Eissa, M.S.; Al-Ansary, H.; Orfi, J.; Elsamni, O.; El-Leathy, A. Examination of Using Aluminum-Foam/Finned-Tube Beds Packed with Maxsorb III for Adsorption Ice Production System. *Energies* **2022**, *15*, 2757. [CrossRef]
- Azurspace. The Use of the Concentrated Sun: Concentrator Triple Junction Solar Cell. 2021. Available online: <https://www.azurspace.com/index.php/en/products/products-cpv/cpv-solar-cells> (accessed on 10 February 2022).
- Zhuang, Z.; Yu, F. Optimization design of hybrid Fresnel-based concentrator for generating uniformity irradiance with the broad solar spectrum. *Opt. Laser Technol.* **2014**, *60*, 27–33. [CrossRef]
- Leutz, R.; Suzuki, A. *Nonimaging Fresnel Lenses: Design and Performance of Solar Concentrators*; Springer: Berlin/Heidelberg, Germany, 2012.

29. Fresnel Factory. Fresnel Lens Suppliers: Technical Information. 2022. Available online: <https://www.fresnelfactory.com/cpv-cell-cpv-panel-cp250-25248-cpv-f250mm-fresnel-lens-suppliers.html> (accessed on 12 February 2022).
30. Shatnawi, H.; Aldossary, A. Outdoor Investigation of High Concentrator Photovoltaic Under Uniform and Non-Uniform Illumination. *J. Daylighting* **2020**, *7*, 1–12. [[CrossRef](#)]
31. Hassanzadeh, A.; Jiang, L.; Winston, R. Coupled optical-thermal modeling, design and experimental testing of a novel medium-temperature solar thermal collector with pentagon absorber. *Sol. Energy* **2018**, *173*, 1248–1261. [[CrossRef](#)]
32. Kerzmann, T.; Schaefer, L. System simulation of a linear concentrating photovoltaic system with an active cooling system. *Renew. Energy* **2012**, *41*, 254–261. [[CrossRef](#)]
33. Evans, D.L. Simplified method for predicting photovoltaic array output. *Sol. Energy* **1981**, *27*, 555–560. [[CrossRef](#)]
34. Wu, L.; Zhao, B.; Ao, X.; Yang, H.; Ren, X.; Yu, Q.; Guo, K.; Hu, M.; Pei, G. Performance analysis of the aerogel-based PV/T collector: A numerical study. *Sol. Energy* **2021**, *228*, 339–348. [[CrossRef](#)]
35. European Commission. Photovoltaic Geographical Information System. 2022. Available online: https://re.jrc.ec.europa.eu/pvg_tools/en/#api_5.2 (accessed on 20 February 2022).
36. Rejeb, O.; Radwan, A.; Abo-Zahhad, E.M.; Ghenai, C.; Serageldin, A.A.; Ahmed, M.; El-Shazly, A.A.; Bettayeb, M.; Abdelrehim, O. Numerical analysis of passive cooled ultra-high concentrator photovoltaic cell using optimal heat spreader design. *Case Stud. Therm. Eng.* **2020**, *22*, 100757. [[CrossRef](#)]
37. Theristis, M.; Sarmah, N.; Khalid, T.; O'Donovan, T.S. Design and Numerical Analysis of Enhanced Cooling Techniques for a High Concentration Photovoltaic (HCPV) System. In Proceedings of the 27th European Photovoltaic Solar Energy Conference and Exhibition, Frankfurt, Germany, 24–28 September 2012.
38. Levinshtein, M.; Rumyantsev, S.; Shur, M. *Handbook Series on Semiconductor Parameters*; World Scientific: Singapore, 1996.
39. Saha, B.B.; Chakraborty, A.; Koyama, S.; Aristov, Y.I. A new generation cooling device employing CaCl₂-in-silica gel–water system. *Int. J. Heat Mass Transf.* **2009**, *52*, 516–524. [[CrossRef](#)]
40. El-Sharkawy, I.; AbdelMeguid, H.; Saha, B. Towards an optimal performance of adsorption chillers: Reallocation of adsorption/desorption cycle times. *Int. J. Heat Mass Transf.* **2013**, *63*, 171–182. [[CrossRef](#)]
41. Jribi, S.; Miyazaki, T.; Saha, B.B.; Koyama, S.; Maeda, S.; Maruyama, T. Corrected adsorption rate model of activated carbon–ethanol pair by means of CFD simulation. *Int. J. Refrig.* **2016**, *71*, 60–68. [[CrossRef](#)]
42. El-Sharkawy, I.I.; Uddin, K.; Miyazaki, T.; Saha, B.B.; Koyama, S.; Miyawaki, J.; Yoon, S.-H. Adsorption of ethanol onto parent and surface treated activated carbon powders. *Int. J. Heat Mass Transf.* **2014**, *73*, 445–455. [[CrossRef](#)]
43. Elsheniti, M.B.; Hassab, M.A.; Attia, A.-E. Examination of effects of operating and geometric parameters on the performance of a two-bed adsorption chiller. *Appl. Therm. Eng.* **2018**, *146*, 674–687. [[CrossRef](#)]
44. Emerson. Copeland Scroll™ 1-5 HP ZPK5. 2022. Available online: <https://climate.emerson.com/en-us/shop/1/copeland-skup42k5e-pfv-800> (accessed on 10 March 2022).
45. Aldossary, A.; Mahmoud, S.; Al-Dadah, R. Technical feasibility study of passive and active cooling for concentrator PV in harsh environment. *Appl. Therm. Eng.* **2016**, *100*, 490–500. [[CrossRef](#)]
46. Wu, Y.; Cui, J.; Xu, X.; Deng, D. Experimental study on active cooling for concentrating photovoltaic cells working at high concentration ratios. *Int. J. Energy Res.* **2021**, *45*, 10682–10695. [[CrossRef](#)]
47. Wang, Y.; Li, M.; Du, W.; Ji, X.; Xu, L. Experimental investigation of a solar-powered adsorption refrigeration system with the enhancing desorption. *Energy Convers. Manag.* **2018**, *155*, 253–261. [[CrossRef](#)]
48. Papoutsis, E.; Koronaki, I.; Papaefthimiou, V. Numerical simulation and parametric study of different types of solar cooling systems under Mediterranean climatic conditions. *Energy Build.* **2017**, *138*, 601–611. [[CrossRef](#)]
49. Xu, D.; Liu, J.; Yan, X.-G.; Yan, W. A Novel Adaptive Neural Network Constrained Control for a Multi-Area Interconnected Power System with Hybrid Energy Storage. *IEEE Trans. Ind. Electron.* **2017**, *65*, 6625–6634. [[CrossRef](#)]

Disclaimer/Publisher's Note: The statements, opinions and data contained in all publications are solely those of the individual author(s) and contributor(s) and not of MDPI and/or the editor(s). MDPI and/or the editor(s) disclaim responsibility for any injury to people or property resulting from any ideas, methods, instructions or products referred to in the content.